generally rank among those with the lowest value of the figure of merit. When a contribution to the figure of merit based on the degree to which the model matches a target powder diffraction pattern is included, the success and the robustness of the method are significantly improved. Using solely powder X-ray diffraction and framework density information proves sufficient, in fact, to reproduce a majority of the known zeolite frameworks. The geometrical terms can be adjusted straightforwardly for other classes of structures. The terms based on the degree of match between observed and calculated diffraction data are intrinsically general, and this simulated annealing approach is therefore broadly applicable.

Acknowledgment. We thank R. Rajagopalan, M. M. J. Treacy, and B. P. Flannery for helpful discussions.

Supplementary Material Available: Tables giving the results for those known zeolite frameworks using both geometric and powder X-ray diffraction pattern matching contributions to the zeolite figure of merit (Table III, structures reproduced; Table IV, structures not reproduced) and using only powder X-ray diffraction pattern matching contributions (Table V, structures reproduced; Table VI, structures not reproduced) and Appendix I, C pseudo-code for the simulated annealing procedure (5 pages). Ordering information is given on any current masthead page.

Fluctuations in Zeolite Aperture Dimensions Simulated by Crystal Dynamics

M. W. Deem,† J. M. Newsam,* and J. A. Creighton§

Contribution from Exxon Research and Engineering Company, Route 22 East, Annandale, New Jersey 08801, and BIOSYM Technologies Inc., 9685 Scranton Road, San Diego, California 92121-2777. *Received July 26, 1991*

Abstract: The lattice dynamics of zeolite frameworks have often been suggested to influence the performance of zeolite materials in catalytic and sorptive applications. In a direct study of the influence of the framework dynamics on pore structure, constant volume crystal dynamics methods are used to simulate variations in the aperture dimensions with temperature of the six representative zeolite structure types SOD (sodalite: 6-ring—six oxygen atoms define the aperture), RHO (rho; 8-ring), TON (theta-1; 10-ring), MFI (silicalite; 10-ring), LTL (Linde type L; 12-ring), and *BEA (beta; 12-ring). The framework flexibilities are explicitly modeled by a crystal mechanics force field with parameters taken from quantitative interpretations of Raman and infrared spectroscopic data. These simulations reveal substantial motion of the framework atoms about their equilibrium positions. The variations in the fluctuations of the effective aperture sizes with temperature depend on the framework connectivity, consistent with experimental observation. The frequency spectra of the O-O distances across the apertures reveal generally well defined periodicities in the pore window motion. The definition, extent, and period of the motion depend on the framework connectivity. It is most pronounced in the SOD and RHO frameworks, previously known from experiment to be most susceptible to static framework distortion. The change in cross-sectional area of the 12-ring window in the LTL framework with time is also periodic. a direct demonstration of pore-mouth breathing motion.

Introduction

The windows in zeolite crystal structures[1-3] dictate molecular sieving capabilities and control access to internal sites that are catalytically active or preferred for binding by sorbates. Effective dimensions calculated from crystallographic data, however, are substantially smaller than those deduced from molecular sieving properties.[1] It has long been speculated that this discrepancy reflects in part a thermally activated breathing motion of the zeolite pores.

The molecular sieving properties of a zeolite are readily measured by monitoring sorbate uptake gravimetrically.[1,4,5] When the kinetic diameter of the sorbate approaches that of the cross-sectional area of the largest zeolite apertures, the rate of uptake becomes slow, and the full sorption capacity is generally only achieved at elevated temperatures. Direct measurement of aperture dimensions as a function of temperature is, in principle, possible by diffraction, but the Debye-Waller factors for zeolite framework species derived from diffraction data usually compensate for a variety of other model deficiencies, including the effects of static disorder and inhomogeneity. Furthermore, the averaged diffraction results cannot indicate coupling of the dynamical motions of successive tetrahedra. Direct measurement of framework vibrations using spectroscopic techniques is possible, although it is only recently that proper lattice dynamical models for the complex structures of zeolites have been pursued. Crystal dynamics techniques have recently been applied to the motion of certain simple molecules within idealized zeolites,[6-13] and some

* Address correspondence to this author at BIOSYM Technologies Inc.
† Present address: Department of Chemical Engineering, University of California, Berkeley, CA 94720.
§ Present address: Chemical Laboratories, University of Kent, Canterbury CT2 7NH, England.

(1) Breck, D. W. *Zeolite Molecular Sieves: Structure, Chemistry and Use*; Wiley and Sons (reprinted by R. E. Krieger, Malabar FL, 1984): London, 1973.
(2) Barrer, R. M. *Hydrothermal Chemistry of Zeolites*; Academic Press: London, 1982.
(3) Newsam, J. M. *Science* **1986**, *231*, 1093-1099.
(4) Barrer, R. M. *Zeolites and Clay Minerals as Sorbents and Molecular Sieves*; Academic Press: London, 1978.
(5) Ruthven, D. M. *Principles of Adsorption and Adsorption Processes*; Wiley-Interscience: New York, 1984.
(6) Demontis, P.; Suffritti, G. B.; Alberti, A.; Quartieri, S.; Fois, E. S.; Gamba, A. *Gazz. Chim. Ital.* **1986**, *116*, 459-466.
(7) Demontis, P.; Suffritti, G. B.; Quartieri, S.; Fois, E. S.; Gamba, A. *Zeolites* **1987**, *7*, 522-527.
(8) Demontis, P.; Suffritti, G. B.; Quartieri, S.; Fois, E. S.; Gamba, A. In *Dynamics of Molecular Crystals*; Lascombe, J., Ed.; Elsevier: Amsterdam, 1987; Vol. 92, pp 699-704.
(9) Demontis, P.; Suffritti, G. B.; Quartieri, S.; Fois, E. S.; Gamba, A. *J. Phys. Chem.* **1988**, *92*, 867-871.
(10) Demontis, P.; Yashonath, S.; Klein, M. L. *J. Phys. Chem.* **1989**, *93*, 5016-5019.
(11) Yashonath, S.; Demontis, P.; Klein, M. L. *Chem. Phys. Lett.* **1988**, *153*, 551-556.
(12) Demontis, P.; Fois, E. S.; Suffritti, G. B.; Quartieri, S. *J. Phys. Chem.* **1990**, *94*, 4329-4334.

0002-7863/92/1514-7198$03.00/0 © 1992 American Chemical Society

progress toward accommodating framework flexibility has been made.[12,14-20] We outline here a general simulations protocol for studies of flexible zeolite frameworks and describe crystal dynamics simulations of six representative zeolite structure types. The framework flexibilities are explicitly modeled in crystal dynamics simulations by a crystal mechanics force field with parameters taken from quantitative interpretations of Raman and infrared spectroscopic data.

Simulations

We have developed a general crystal mechanics system for simulating microporous framework structures in which the total classical potential energy is described as

$$U(\mathbf{x},...,\mathbf{x}_n) = \frac{1}{2}\sum_i \sum_{j=1}^{\text{bonds}(i)} \left\{ \frac{1}{2}\gamma_{ij}[|\mathbf{x}_i - \mathbf{x}_j| - x_{ij}^0]^2 + \sum_{k=1}^{j-1} \beta_{jik}[\theta(\mathbf{x}_j,\mathbf{x}_i,\mathbf{x}_k) - \theta_{jik}^0]^2 \right\} + \frac{1}{2}\lim_{L\to\infty} \frac{1}{4\pi\epsilon_0} \sum_{i,j,\mathbf{l}}' \frac{q_i q_j}{|\mathbf{x}_i - (\mathbf{x}_j + \mathbf{l})|} - \frac{1}{4\pi\epsilon_0}\sum_i \frac{1}{2}\alpha_i |\mathbf{E}(\mathbf{x}_i)|^2 + \frac{1}{2}\sum_{i,j,\mathbf{l}}' \left[\frac{A_{ij}}{|\mathbf{x}_i - (\mathbf{x}_j + \mathbf{l})|^{12}} - \frac{B_{ij}}{|\mathbf{x}_i - (\mathbf{x}_j + \mathbf{l})|^6} \right] \quad (1)$$

$$\mathbf{l} \in V(L)$$

Periodic boundary conditions are implicit. Each term in this sum represents one component of the energy associated with an ionic or molecular crystal. For a zeolite, this energy expression applies to the entire system, including nonframework and sorbate species if desired. For the detailed crystal mechanics results discussed further below, only the bond stretch and bond angle bend terms, defined by the respective force constants γ_{ij} and β_{jik}, are taken as non-zero. However, the same description (1) can be used to study cation or sorbate dynamics, or to apply different effective potential functions. For example, by restricting the ranges of i and j, the Coulomb and the Lennard-Jones terms, the second and fourth terms respectively in (1), can be structured to simulate framework–framework, framework–sorbate, or sorbate–sorbate interactions. Setting γ_{ij} and β_{jik} to zero and including the framework–framework Coulomb and Lennard-Jones terms, for example, produces the type of rigid-ion potential developed by Kramer et al.[21], Setting γ_{ij} to zero but retaining an O–T–O bond bend term as β_{jik} and the Coulomb and Lennard-Jones terms gives the type of rigid-ion potential applied to silicates and zeolites by Catlow et al.[22] The third term, quadratic in the electric field, provides a simple treatment of isotropic atomic polarization in which corrections to the electric field generated by such polarization are not included in eq 1. This approximation should be reasonably accurate except, perhaps, for neutral, highly polarizable sorbates. The shell model has been used previously to treat framework oxygen atom polarizability in static zeolite systems,[22] but a full explicit treatment of atomic polarization in crystal dynamics simulations involves a substantial computational burden.

Numerical implementation of eq 1 requires consideration of the convergence properties with distance of the various terms. The atom positions are defined by $\mathbf{x}_i + \mathbf{l}$, where $\mathbf{x}_i$ is the position in a unit cell, and $\mathbf{l}$ is the origin of that particular unit cell. The fourth, Lennard-Jones term is a well-defined, absolutely convergent sum which can, therefore, be evaluated to within a given tolerance by terminating the computation when the distance between interacting atoms exceeds a specified cutoff. The crystal sum of the third, Coulomb term is evaluated in a computationally viable fashion by the Ewald method,

$$S = \frac{1}{2}\lim_{L\to\infty} \sum_{i,j,\mathbf{l}}' \frac{q_i q_j}{|\mathbf{x}_i - (\mathbf{l} + \mathbf{x}_j)|} = \frac{1}{2}\sum_{i,j,\mathbf{l}}' q_i q_j \frac{\text{erfc}\,(\alpha x_{i,j,\mathbf{l}})}{x_{i,j,\mathbf{l}}} + \frac{1}{2\pi U}\sum_{\mathbf{h}\neq 0} |F(\mathbf{h})|^2 \frac{e^{-\pi^2 h^2/\alpha^2}}{h^2} - \frac{\alpha}{\sqrt{\pi}}\sum_i q_i^2 + \frac{1}{2U}\int_{\partial V(L)} \frac{\mathbf{d.r}\ \mathbf{d.n}}{\mathbf{x}^3}\, dS \quad (2)$$

in which the last term, which is non-zero only for non-centrosymmetric crystal structures and represents physically a surface charge interaction,[23] is ignored. Only one of the structures considered below is non-centrosymmetric.

The code is configured to handle the general potential, eq 1. All parameters required by the component expressions are user-input and identified by name$_i$, name$_j$ (=that for name$_j$, name$_i$); or name$_j$, name$_i$, name$_k$ (=name$_k$, name$_i$, name$_j$). Bonds and angle connections are computed from the initial structure, with the framework atom connectivity fixed throughout the simulation. A grid is built to allow 3-dimensional searching in linear time.[24] The grid is defined so that all atoms within r_{max} of an atom can be found by searching the box the atom is in and its 26 nearest neighbors. Considerable computational speed-up can be realized on optimizing the grid building. For example, if the grid boxes are made r_{excess} too large, the grid need be rebuilt at most only every r_{excess}/r_{shift} framework perturbations, where r_{shift} is the maximum possible coordinate shift in a given iteration (although this option is not used in the present crystal dynamics simulations). Choosing a value of r_{max} also implies values of α and h_{max} necessary to achieve a given accuracy in eq 2. Typically, it is eq 2 that consumes the greatest amount of CPU time if Coulomb interactions are incorporated. For methane in zeolite L, with Coulomb and Lennard-Jones framework–sorbate and sorbate–sorbate interactions, 60% of the burden of evaluating eq 1 is due to evaluation of eq 2.

Crystal dynamics[25] requires computation of the force on each atom, defined by

$$\mathbf{F}_i = -\nabla_i U(\mathbf{x}_1,...,\mathbf{x}_n) \quad (3)$$

the gradient being computed analytically (but checked numerically at the outset). The use of periodic boundary conditions implies that atoms related by translational periodicity exert no force on each other. The equations of motion to be solved numerically are then

$$d\mathbf{x}_i/dt = \dot{\mathbf{x}}_i$$

$$d\dot{\mathbf{x}}_i/dt = \mathbf{F}_i/m$$

$$\mathbf{x}_i(0) = \mathbf{x}_i^0; \qquad \dot{\mathbf{x}}_i(0) = \mathbf{v}_i^0 \quad (4)$$

The initial positions, $\mathbf{x}_i^0$ are user input, and the initial velocities are assigned randomly on the basis of a defined total input energy value and such that the total framework linear momentum is zero.

(13) Cohen de Lara, E.; Kahn, R.; Goulay, A. M. *J. Chem. Phys.* **1989**, *90*, 7482–7491.
(14) Shin, J. M.; No, K. T.; Jhon, M. S. *J. Phys. Chem.* **1988**, *92*, 4533–4540.
(15) Song, M. K.; Shin, J. M.; Chon, H.; Jhon, M. S. *J. Phys. Chem.* **1989**, *93*, 6463–6468.
(16) Van Santen, R. A.; Vogel, D. L. In *Advances in Solids State Chemistry*; Catlow, C. R. A., Ed.; JAI Press: London, 1989; Vol. 1, pp 151–224.
(17) Miyamoto, A.; Matsuba, K.; Kubo, M.; Kawamura, K.; Inui, T. *Chem. Lett.* **1991**, 2055–2058.
(18) Van Santen, R. A.; de Man, A. J. M.; Jacobs, W. P. J. H.; Teunissen, E. H.; Kramer, G. J. *Catal. Lett.* **1991**, *9*, 273–286.
(19) Nicholas, J. B.; Hopfinger, A. J.; Trouw, F. R.; Iton, L. E. *J. Am. Chem. Soc.* **1991**, 4792–4800.
(20) Catlow, C. R. A.; Freeman, C. M.; Vessal, B.; Tomlinson, S. M.; Leslie, M. In *Science and Engineering on Supercomputers*; Pitcher, E. J., Ed.; Computational Mechanics Publications: Boston and Springer-Verlag: Berlin, 1990; pp 385–393.
(21) Kramer, G. J.; Farragher, N. P.; van Beest, B. W. H.; van Santen, R. A. *Phys. Rev. B* **1991**, *43*, 5068–5080.
(22) Jackson, R. A.; Catlow, C. R. A. *Molecular Simulations* **1988**, *1*, 207–244.
(23) Deem, M. W.; Newsam, J. M.; Sinha, S. K. *J. Phys. Chem.* **1990**, *94*, 8356–8359.
(24) Sedgewick, R. *Algorithms*, 2nd ed.; Addison-Wesley: Reading, MA, 1988.
(25) Allen, M. P.; Tildesley, D. *Molecular Simulation of Liquids*; Oxford University Press: Oxford, 1980.

The presence of the bonding terms in eq 1 causes the solution to eq 4 to be highly oscillatory. We thus use VODE, a variable-order, variable stepsize integrator designed to deal with difficult to integrate, nonlinear ordinary differential equations.[26-31] This code is, for example, 2.5 times as fast as a Bulirsch-Stoer integrator[32] on eq 4 for four significant figure accuracy. A simpler example problem illustrates the superiority of a sophisticated integrator over an Eulerian integrator.[32]

$$dy/dt = \dot{y}$$

$$d\dot{y}/dt = -y$$

$$y(0) = 0; \qquad \dot{y}(0) = 1 \tag{5}$$

The VODE algorithm is 10^5 times as fast as Euler's method in calculating $y(100)$ (=sin 100) to, say, three significant figures. VODE also requires 15 times fewer function evaluations to achieve this level of accuracy than does the velocity Verlet method.[25,33] VODE provides the capability of using the second derivative matrix. On a test problem of masses connected to their nearest neighbors by a Hookeian, 1-dimensional spring, use of this option speeded up the integration by 40%. Since computation of the Jacobian of eq 1 would be relatively time consuming, this feature of VODE is not currently exploited. VODE allows for input relative (r_{tol}) and absolute (a_{tol}) error tolerances. We typically specify $r_{tol} = 10^{-5}$ and $a_{tol} = 10^{-7}$, which imply 5 significant figure accuracy for integration over a reasonable time range.

The velocity enters the total Hamiltonian as the sum of independent squared velocities, and the classical equipartition theorem states

$$\tfrac{1}{2}(\sum_i m_i|\dot{\mathbf{x}}_i|^2) = \tfrac{3}{2}NkT \tag{6}$$

defining the temperature of the system. In fact, it follows that the velocities are three-dimensional Gaussian. The ensemble implied by eq 1 is the constant N, E, and V microcanonical ensemble.

To apply eq 1 as a crystal mechanics description for studying zeolite framework flexing in which Coulomb, Lennard-Jones, and polarization contributions to the energy are omitted requires accurate values for the force constants, equilibrium bond lengths and angles, and atomic masses. The equilibrium framework structural data are taken from published refinements (based on diffraction data) of silica sodalite (SOD[34]), silica ZSM-22 (TON[35]), ZSM-5 (MFI[36]), potassium zeolite L (LTL[37]) and (based on distance least-squares refinements) RHO,[38] LTL,[38] and *BEA[39] framework structures. In ZSM-22, for example, there is more than one bonding distance between certain crystallographically unique atoms, requiring special consideration in the definitions of the x_{ij}^0 and Θ_{jik}^0 in eq 1.

Table I. Force Constants Used in Equation 1

Si–O:	5.0×10^{-18} J m^{-2}
O–Si–O:	1.35×10^{-18} J rad^{-2}
Si–O–Si:	0.31×10^{-18} J rad^{-2}

The force constants α_{ij} and β_{jik} are calculated from experimentally determined vibration frequencies of the aluminosilicate framework in the sodalite $Na_8[Al_6Si_6O_{24}]Cl_2$ as discussed in the literature elsewhere.[40,41] For the sodalite framework the three totally symmetric, zero-wave-vector modes depend only on the mean T–O stretching and O–T–O and T–O–T bending force constants, where T = Si or Al.[40] These force constants are, therefore, uniquely determined from the measured Raman spectra. An adaptation of the GF matrix method[42] is used to calculate the frequencies of the asymmetric, zero-wave-vector modes,[41] which depend on the individual Si–O and Al–O stretching and O–Si–O and O–Al–O bending force constants. The GF matrix method essentially reduces equation 1 to quadratic terms about equilibrium and then applies harmonic oscillator theory. The force constants are thus determined by adjusting their values so that the calculated and experimental spectra agree. Exact matching is not possible without including off-diagonal force constants in the F matrix. These terms, which are the coefficients in the potential energy function of $[|\mathbf{x}_i - \mathbf{x}_j| - x_{ij}^0][\Theta(\mathbf{x}_j,\mathbf{x}_i,\mathbf{x}_k) - \Theta_{jik}^0]$, are generally small, and they are not included in eq 1. With the force constant values given in Table I, all of the bands in the Raman and infrared spectra of lithium, sodium, and potassium chloride sodalites are reproduced to within 50 cm^{-1}. While inexact, this level of agreement, ~4% for the highest frequency modes, is reasonable, and it is substantially better than that obtained with rigid-ion or shell model potentials.[18,20,43] The values of the force constants listed in Table I are similar to those reported in other quantitative studies of silicate structures.[40] For example, the mechanics potential of Etchepare et al. for quartz has constants of 5.943 J m^{-2}, 0.729 $\times 10^{-18}$ J rad^{-2}, and 0.126 $\times 10^{-18}$ J rad^{-2} respectively for the Si–O stretch and O–Si–O and Si–O–Si bend terms.[44]

Results

For each of the six framework types, crystal dynamics simulations are performed at 4 or 5 temperatures so that the evolution in the lattice dynamics can be tracked. In each case the crystallographic data are taken as input, the atomic contents of a complete unit cell being generated from the associated symmetry operations. These atoms are treated independently in the simulations, the crystallographic unit cell being the basis of the periodic boundary conditions. An approximate target temperature is defined by the total kinetic energy to be introduced into this equilibrium state, apportioned across all of the framework atoms such that the total linear momentum is zero. Simulations are performed from 0 to 20 ps, in steps of 0.01 ps. Each time step typically involved 64 gradient evaluations in VODE in order to obtain the level of 5 significant figure accuracy for the integration required by the specified error tolerances. The output time step has nothing to do with the accuracy of the solution of the system of differential equations and is chosen simply to provide an adequate number of configurations for statistical analysis. The full set of atomic coordinates is stored after each time step and analyses are performed on the 2–20-ps sections, the first 2 ps being allocated to system equilibration. The temperatures given in the table are derived from eq 6 by averaging over the instantaneous temperatures for the 2–20-ps interval. As expected, the temperature scales well with the number of atoms in the system at constant input energy. The calibre of the integrator is evidenced by a typical

(26) Brown, P. N.; Byrne, G. D.; Hindmarsh, A. C. *LLNL Report UCRL-98412* **1988**. *June 1988*; *SIAM J. Sci. Stat. Comput.* **1989**, *10*, 1038–1051.
(27) Byrne, G. D.; Hindmarsh, A. C. *ACM Trans. Math. Software* **1975**, *1*, 71–96.
(28) Hindmarsh, A. C.; Byrne, G. D. *LLNL Report UCID-30112, Rev. 1* **1977**. *April 1977*.
(29) Byrne, G. D.; Hindmarsh, A. C. *LLNL Report UCID-30132* **1976**. *April 1976*.
(30) Hindmarsh, A. C. In *Scientific Computing*; Stepleman, R. S. et al., Ed.; North-Holland: Amsterdam, 1983; pp 55–64.
(31) Jackson, K. R.; Sacks-Davis, R. *ACM Trans. Math. Software* **1980**, *6*, 295–318.
(32) Press, W. H.; Flannery, B. P.; Teukolsky, S. A.; Vetterling, W. T. *Numerical Recipes*; Cambridge University Press: New York, 1989.
(33) Verlet, L. *Phys. Rev.* **1967**, *159*, 98.
(34) Richardson, J. W.; Pluth, J. J.; Smith, J. V.; Dytrych, W. J.; Bibby, D. M. *J. Phys. Chem.* **1988**, *92*, 243–247.
(35) Marler, B. *Zeolites* **1987**, *7*, 393–397.
(36) Van Koningsveld, H.; van Bekkum, H.; Jansen, J. C. *Acta Crystallogr.* **1987**, *B43*, 127–132.
(37) Newsam, J. M. *J. Phys. Chem.* **1989**, *93*, 7689–7694.
(38) Van Genechten, K. A.; Mortier, W. J. *Zeolites* **1988**, *8*, 273–283.
(39) Newsam, J. M.; Treacy, M. M. J.; Koetsier, W. T.; deGruyter, C. B. *Proc. R. Soc. London* **1988**, *A420*, 375–405.
(40) Creighton, J. A.; Deckman, H. W.; Newsam, J. M. *J. Phys. Chem.* **1991**, *95*, 2099–2101.
(41) Creighton, J. A.; Deckman, H. W.; Newsam, J. M. In preparation, 1992.
(42) Shimanouchi, T.; Tsuboi, M.; Miyazawa, T. *J. Chem. Phys.* **1961**, *35*, 1597.
(43) de Man, A. J. M.; van Beest, B. W. H.; Leslie, M.; van Santen, R. A. *J. Phys. Chem.* **1990**, *94*, 2524.
(44) Etchepare, J.; Merian, M.; Smetankine, L. *J. Chem. Phys.* **1974**, *60*, 1873.

relative change in total system energy over the full 20-ps run of less than 0.5%.

The apertures and the pore space within a zeolite framework are bounded by the framework oxygen atoms. For each of the structure types appropriate distances between pairs of oxygen atoms across the various apertures are computed as a function of time throughout the simulations. Depending on the structure type, both of the relevant oxygen atoms in a pair might be independent atoms within the same unit cell, as in the *BEA framework, or, as the LTL framework, one oxygen might require unit cell translations (see Figure 1 and footnotes to Table II). The various distances are then collated to yield histograms of the number of occurrences of a given distance at the various simulation temperatures (Figure 2). The corresponding means and standard deviations are given in Table II. The trajectories are animated using InsightII,[45] with the selected O–O distances being monitored as a function of time through the simulations (Figure 1). Depending on the framework type, these plots reveal that the identified distances evolve at one or more characteristic frequencies. To highlight these frequencies, data for a series of LTL-framework simulations are Fourier transformed to yield the power spectra displayed in Figures 5 and 6.

For each structure type the simulations at each temperature are performed at constant volume, using the same unit cell dimensions at each temperature. Over the same temperature range a series of Monte Carlo simulations is performed for the LTL framework using the same potential parameters (Table I). In these simulations, both framework atomic coordinates and unit cell dimensions are allowed to vary, subject to the constraints of maintaining a metrically trigonal/hexagonal cell, that is $a = b$, $\alpha = \beta = 90°$, and $\gamma = 120°$. The unit cell dimensions are found to vary little with temperature, showing in fact a slight decrease in both a and c over the range 30–550 K. In simple structures, the typically positive thermal expansion can be ascribed to the anharmonicity of the interatomic interactions. A harmonic potential, such as that used here (note that the potential is harmonic in *nonlinear* coordinates in eq 1), is anticipated to give little change in volume with temperature. The small negative thermal expansion coefficient obtained in the present simulations is consistent with that actually measured by diffraction for potassium zeolite L.[37] The negative thermal expansivity, which has since been noted in other simulations,[46] has been rationalized in terms of the flexibility of the framework and in the substantial internal void volume which allows the framework to expand "inwardly" with increasing temperature.[47]

The dependence of the simulation results on the details of the initial model and on the volume of the unit cell is examined by simulations of the LTL framework based on the structure obtained by distance least squares for a silica composition,[38] the structure measured by diffraction for aluminosilicate zeolite L at Si:Al = 2.8,[37] and two supercells, $a \times a \times 3c$ and $2a \times 2a \times c$, with volumes respectively three and four times that of the parent aluminosilicate structure. The results for the two different starting structures are almost identical (Table II). Likewise, the O–O distance histograms for the $a \times a \times c$, $a \times a \times 3c$, and $2a \times 2a \times c$ simulations overlap exactly at 80 K and are quite similar also at 550 K (Figure 7). The appearances of the power spectra (Figures 5 and 6) do change substantially with both temperature and the size of the defined translational repeat unit. The increased number of pronounced modes with temperature, particularly at higher frequencies, is expected on the basis of the greater thermal agitation attained at higher temperatures. The changes in the power spectra associated with the changed unit cell volumes are more pronounced for the $2a \times 2a \times c$ case than for $a \times a \times 3c$, probably because the distances monitored are in the *ab* plane. The marked changes in the power spectra for the larger repeat units are either slight changes in mode frequency or changes in mode intensity. The nature of these changes combined with the similar character of the O–O distance histograms imply that conclusions based on the crystallographic unit cells as the repeating units are likely representative of the structure types. That is, given the already substantial sizes of the zeolite unit cells, the effective pore dimensions do not appear to be affected noticeably by phonons that have wavelengths longer than the unit cell repeat lengths.

Discussion

Animations of the results of the crystal dynamics calculations manifest, even at low temperature, substantial departures of the framework atoms from their equilibrium positions. Inspection reveals that these changes result largely from reorientational motion of successive tetrahedra by rotations about the T–O bonds (T = tetrahedral species, Si in this case), consistent with the significant potential energy penalty for even small changes of intratetrahedral geometry, compared with the large flexibility in the apical oxygen atom linkage between adjacent tetrahedra (Table I). There are no direct experimental data on the extent of motion of the framework atoms in real zeolite materials. The isotropic Debye–Waller factor, B, an atomic variable deduced in fitting measured diffraction data, is, in principle, a measure of the thermally induced departure of an atom from its equilibrium position, being related to the mean squared displacement, $\langle \bar{u}^2 \rangle$, by $B = 8\pi^2\langle \bar{u}^2 \rangle$. The diffraction data for potassium zeolite L at 78 K yield a value for the framework oxygen atoms of $B = 2.4$ Å^2[37] corresponding to $\langle \bar{u}^2 \rangle = 0.030$ Å^2. This B value is reasonably typical of those reported in similar zeolite crystal structure refinements ($\sim$1.0–3.0 Å^2). The average value of $\langle \bar{u}^2 \rangle$ for all 72 framework oxygen atoms in the LTL-framework simulation at 80 K is, however, 0.005 Å^2, much lower than that measured. This is not surprising, for the nature of the diffraction data fitting is such that the optimized B-factor values typically compensate for a variety of other complicating factors present in the real material, such as the effects of framework aluminum, defects, disorder, and inhomogeneity. For precise diffraction studies on high-quality single crystals the measured $\langle \bar{u}^2 \rangle$ values are, as expected, significantly lower, for example, 0.01 Å^2 in basic sodalite at 298 K[48] and 0.006 Å^2 in mineral thomsonite at 13 K.[49] The value reported for silica sodalite, 0.04 Å^2, is, in comparison, somewhat high,[34] suggesting the presence also of some static disorder. Thus, although detailed quantitative comparisons with diffraction data are not possible, the present results give good qualitative agreement. Despite the apparently large thermal fluctuations in the framework atom positions, the mean squared displacements are, as expected, substantially smaller than the upper limit afforded by diffraction results.

The effect of the motion of the framework atoms on the pore dimensions depends on the framework type. To illustrate graphically the pore window breathing motion, the cross-sectional area (CSA) of the 12-ring window in the LTL framework in projection along [001] was calculated for the SiO_2 composition at each frame of the crystal dynamics simulation (Figure 8). The CSA is approximated as the area of the polygon inscribed within the projection of the van der Waals spheres of the 12 oxygen atoms defining the window along [001]. The 12 oxygen atoms defining the 12-ring window are all independent in the simulation. The CSA displays a regular, cyclical variation at a frequency of $\sim$200 cm^{-1}. This is a clear and direct demonstration of breathing motion of the zeolite pores. The breathing motion frequency varies little with temperature, although definition of the motion becomes less clear at higher temperatures (Figure 8). The peak–trough difference in area at 550 K corresponds to a maximum fluctuation in pore diameter of about 0.3 Å. This fluctuation in CSA is a multibody effect.

The data in Table II and Figure 4 illustrate that the effect of increasing temperature on the pore apertures depends on the framework type. For the LTL framework of zeolite L, for ex-

(45) *InsightII User and Reference Guides*; Biosym Technologies Inc., 1991.
(46) Jackson, R. A.; Parker, S. C.; Tschaufeser, P. In *Modelling of Structure and Reactivity in Zeolites*; Catlow, C. R. A., Ed.; Academic Press: London, 1992; pp 43–61.
(47) Barrer, R. M. Private communication, 1989.
(48) Hassan, I.; Grundy, H. D. *Acta Crystallogr.* **1983**, *C39*, 3–5.
(49) Ståhl, K.; Kvick, Å.; Smith, J. V. *Acta Crystallogr.* **1990**, *C46*, 1370–1373.

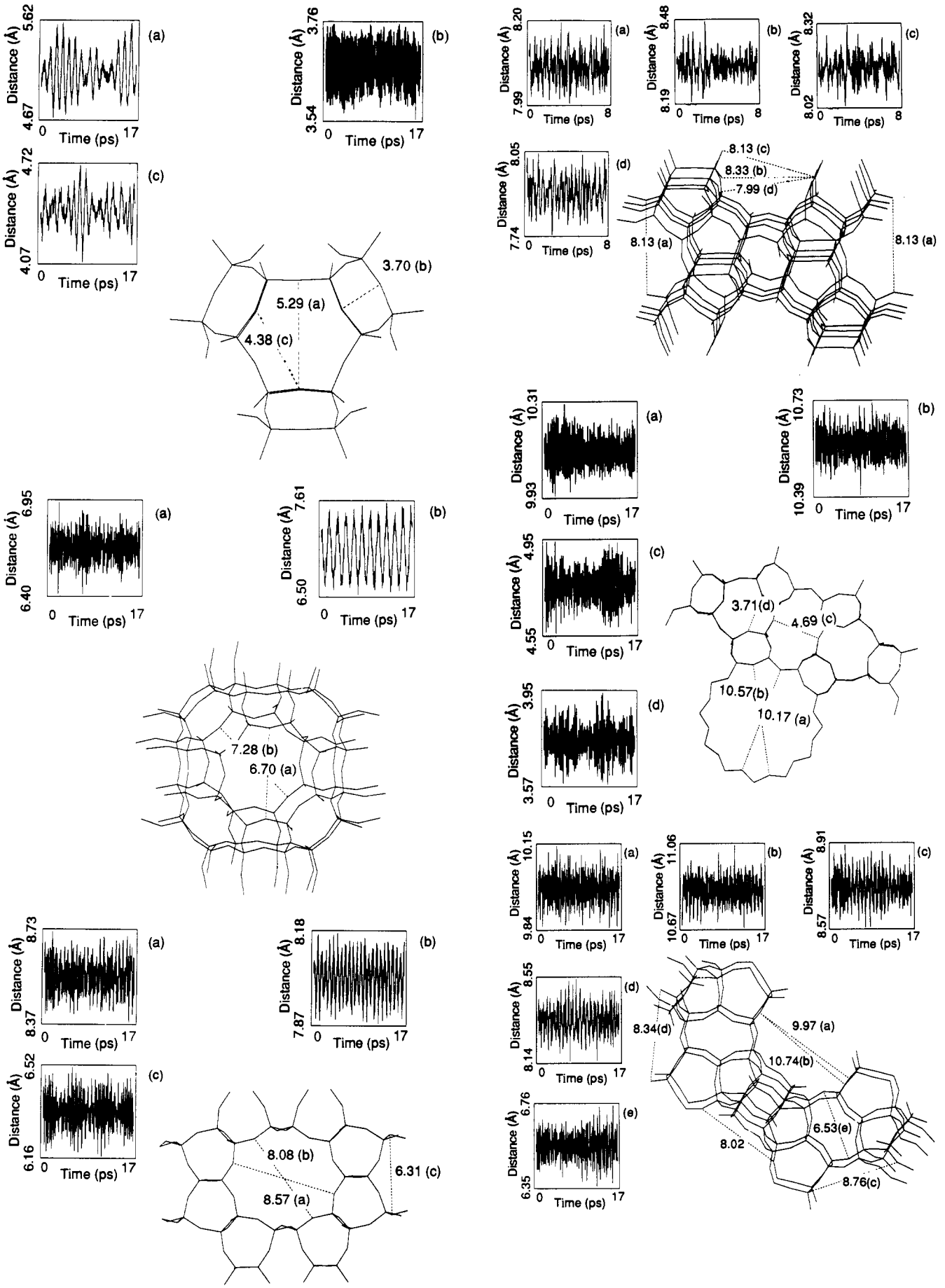

Figure 1. Representations of the structures SOD (top left), RHO (center left), TON (lower left), MFI (top right), LTL (center right), and *BEA (lower right) studied in the text. Also illustrated are the time evolutions of selected O–O separations at the lowest temperature studied in each case.

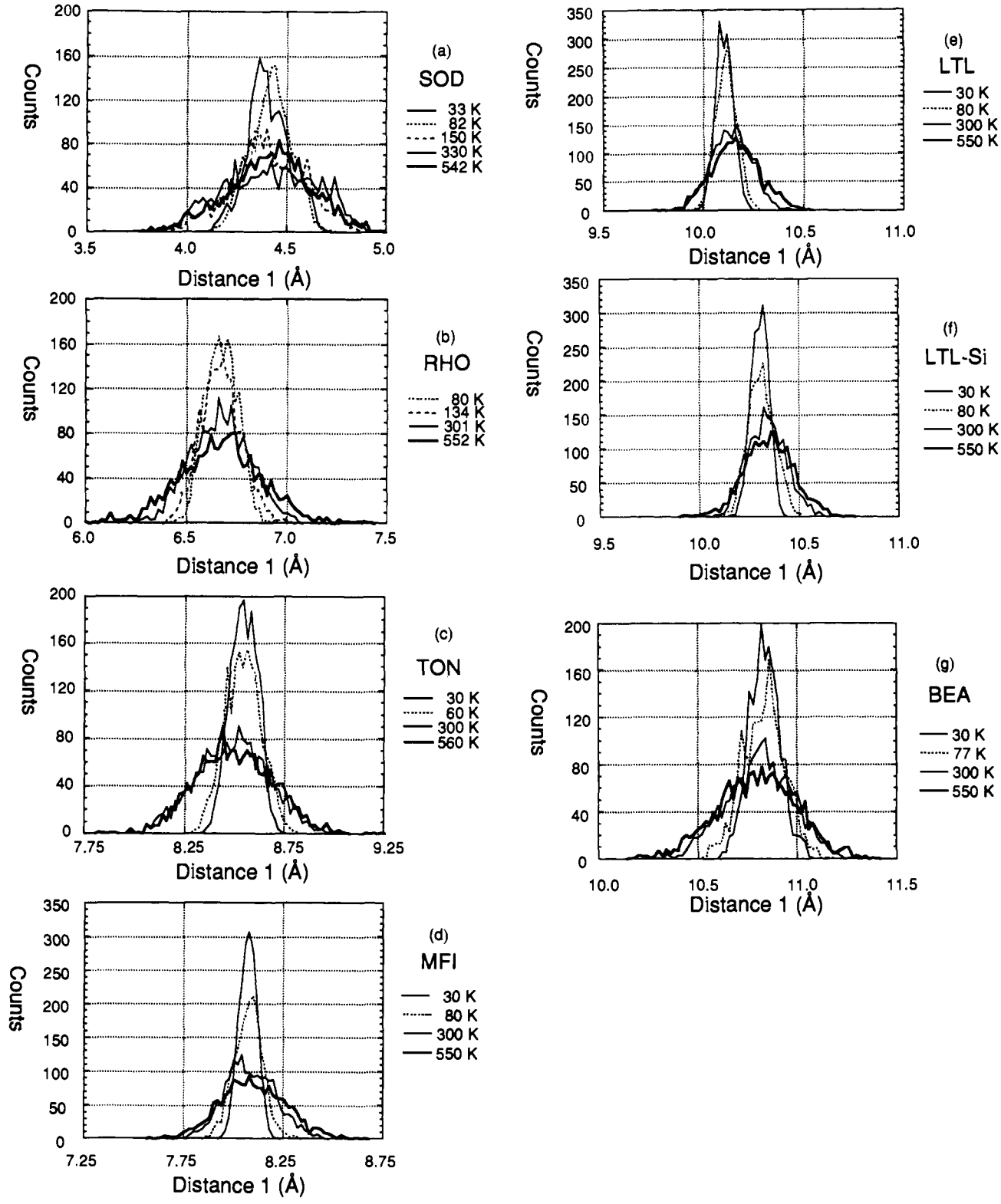

Figure 2. Histograms of O–O separations across the apertures of SOD (a, 6-ring), RHO (b, 8-ring), TON (c, 10-ring), MFI (d, 10-ring), LTL (e, 12-ring), purely siliceous LTL (f, 12-ring), and *BEA (g, 12-ring) structures at various simulation temperatures. In all cases, the data that generated mean 1 in Table II are plotted. The plots show 1800 data, spanning the 2–20-ps segments of 20-ps runs in 0.01-ps steps. Typical 20-ps runs consumed 954 s (LTL) and 1265 s (*BEA) of Cray X-MP/14se CPU time. A typical 20-ps LTL run consumes 12300 s on a 36 MHz Silicon Graphics Personal Iris 4D/35.

ample, the mean 12-ring O–O separation shows a steady increase with temperature, whereas the mean 8-ring O–O separation in the RHO framework is invariant (Figure 4). These differences reflect the differing connectivities of the silicate tetrahedra, although we have not attempted to analyze in detail how a given framework connectivity gives rise to the observed evolution. A simple inspection, however, reveals some interesting features. In the case of the RHO framework, the plots in Figure 3 illustrate that at low temperature there are two distinct preferred conformations; these correspond to the two possible directions for the elliptical distortion of the pore windows.[50,51]

(50) Baur, W. H.; Fischer, R. X.; Shannon, R. D. In *Innovations in Zeolite Material Science* Grobet, P. J., Mortier, W. J., Vansant, E. F., Schulz-Ekloff, G. Eds.; Elsevier: Amsterdam, 1987; Stud. Surf. Sci. Catal. No. 37; pp 281–292.

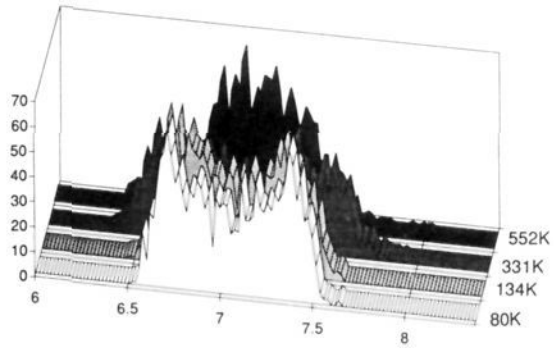

Figure 3. Histograms of the O–O separation in the RHO framework that generated mean 2 in Table II. The histograms are for the four temperatures of Table II.

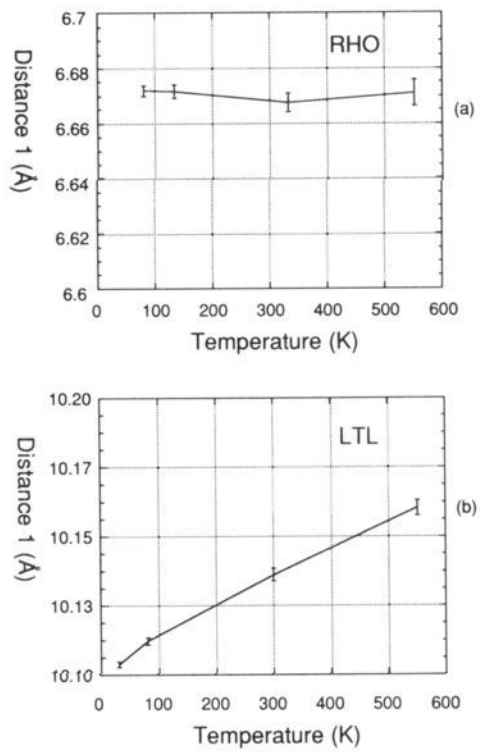

Figure 4. Mean and error bars (=std/$\sqrt{1800}$) of the O–O separations across the apertures of RHO (a, 8-ring) and LTL (b, 12-ring) framework structures as a function of simulation temperature. In all cases, the data that generated mean 1 in Table II are plotted.

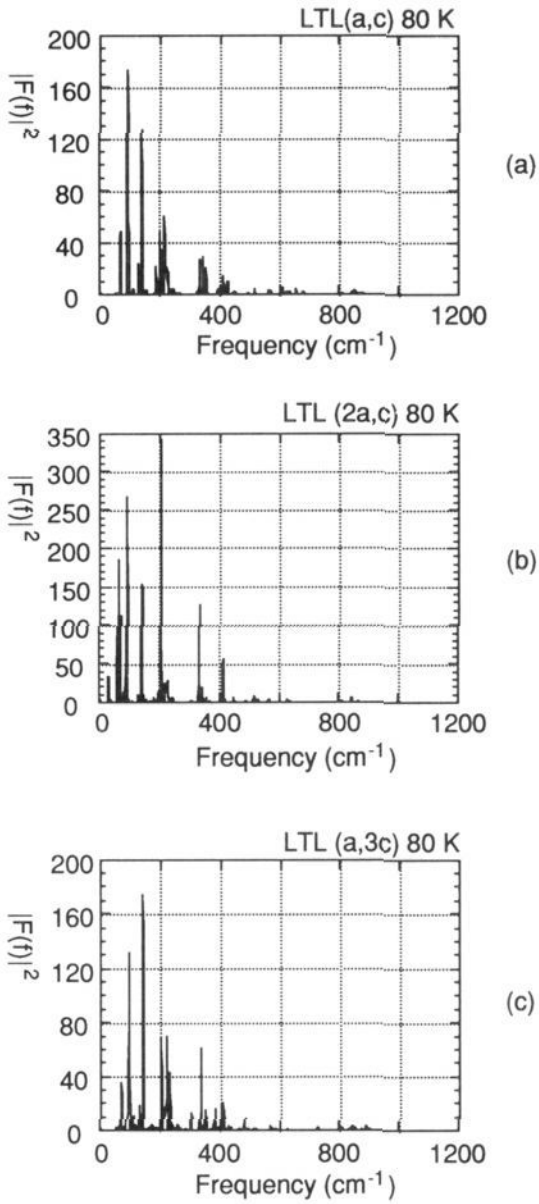

Figure 5. Power spectra for representative O–O separations across the 12-ring aperture of the LTL framework with the simulations at 80 K based on the crystallographic unit cell (a: a = 18.5 Å, c = 7.5 Å), on a $2a \times 2a \times c$ cell (b: a = 37.0 Å, c = 7.5 Å), and on a $a \times a \times 3c$ cell (c: a = 18.5 Å, c = 22.5 Å). In all cases, the data that generated mean 1 in Table II are used.

The plots of O–O distance across the apertures as a function of time in the simulation shown in Figure 1 reveal strikingly marked fluctuations in the geometry of the zeolite pores. Particularly in the SOD and RHO frameworks at low temperature there is a well-defined periodicity to the temporal variation in the O–O distances across the 6- and 8-rings. The potentials used in the present simulations involve only short-range, first-neighbor terms, and these simulation data must thus, as above, reflect the modes of coupling of the tetrahedra linked through the framework connectivities. This coupling and the character of the breathing modes indeed depend quite sensitively on the structure type.

The extent of the variation in the O–O separations along the diagonals of the 8-ring windows in the RHO framework is about twice that found across the 10-ring windows of the MFI framework and the 12-ring windows of the LTL and *BEA frameworks (Figure 3 and Table II). The RHO framework is known, based on both the properties of physical models and crystallographic evidence, to be particularly flexible. The most pronounced distortion mode observed in these simulations, elongation–contraction or elliptical distortion of the 8-ring diagonal (Figure 1), is exactly that observed crystallographically as the nonframework or framework composition is changed.[50,51] The framework motions will not be affected to first order by the presence of sorbed species. A more rigorous calculation of the statistical mechanical properties of the zeolite system containing additional adsorbed species would be possible using perturbation theory applied to the reference motions we present.[52]

The pattern of change of the distribution of aperture O–O distances with temperature is broadly consistent with that expected on the basis of experimental sorption data.[1] A discrepancy between the static effective dimensions calculated from crystallographic data and those deduced from molecular sieving properties at finite temperature reflects the kinetic energy of the sorbate molecules,

(51) Corbin, D. R.; Abrams, L.; Jones, G. A.; Eddy, M. M.; Stucky, G. D.; Cox, D. E. *J. Chem. Soc., Chem. Commun.* **1989**, 42–43.

(52) Chandler, D. *An Introduction to Modern Statistical Mechanics*; Oxford: New York, 1987.

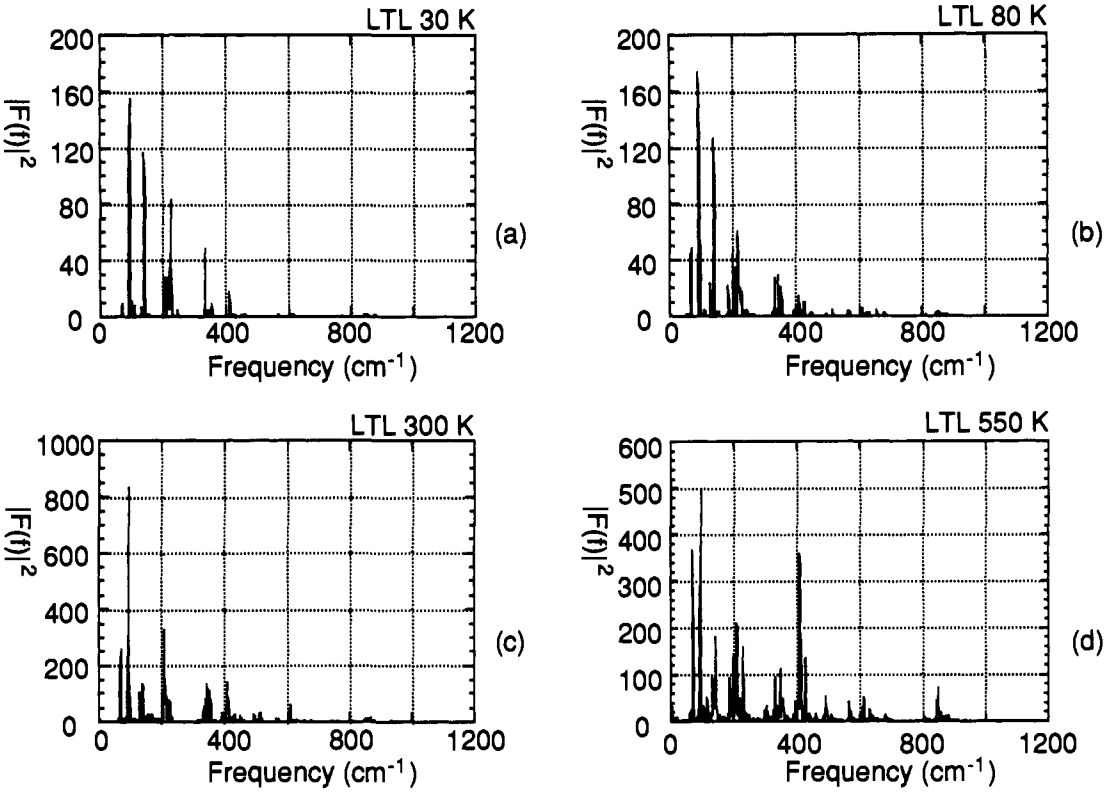

Figure 6. Power spectra for representative O–O separations across the 12-ring aperture of the LTL framework for simulations based on the crystallographic unit cell (a = 18.5 Å, c = 7.5 Å) at 30 (a), 80 (b), 300 (c), and 550 K (d). In all cases, the data that generated mean 1 in Table II are analyzed.

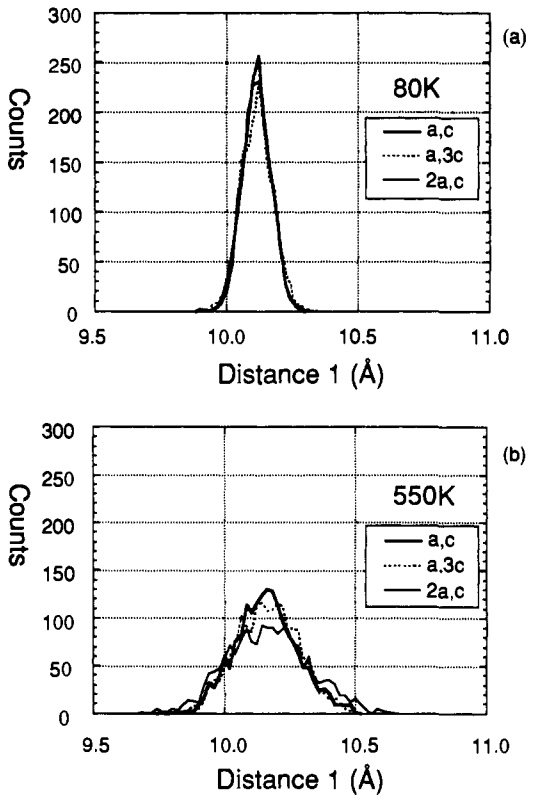

Figure 7. Histograms of O–O separations across the aperture of the LTL framework structure for the three unit cell sizes of Figure 3, at the nominal temperatures of 80 (a) and 550 K (b). In all cases, the data that generated mean 1 in Table II are plotted.

the fact that the sorbate and zeolite aperture atoms are not hard, rigid spheres, and the cooperative breathing motion of the framework revealed by the present simulations. A reduced activation barrier to passage of a molecule through a zeolite aperture with temperature reflects in part the increased framework breathing motion.

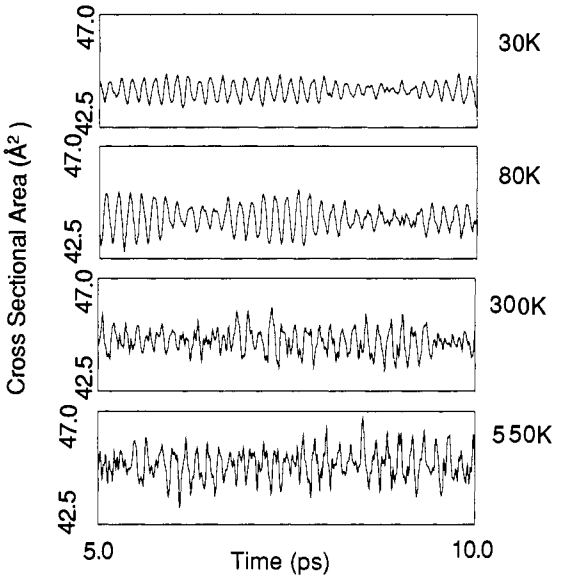

Figure 8. Time evolution of the cross-sectional area of the 12-ring window in the LTL framework at 30, 80, 300, and 550 K.

An issue in geometrical interpretations of simulations of this type is the appropriateness of using classical mechanics in eq 1, the results of which may deviate significantly from quantum mechanical predictions. For a one-dimensional oscillator, or one of the independent directions of an n-dimensional oscillator, the ground state *wave function* density is a Gaussian. The *classical* density of a single oscillator with amplitude a is, however,

$$\rho(x)\,dx = \frac{1}{\pi a}\frac{1}{\sqrt{1-(x/a)^2}}\,dx \qquad (7)$$

Table II. O–O Separations across the Apertures as a Function of Temperature

(a) SOD Framework: A 6-Ring System

	temp (K)						temp (K)				
	33	82	150	330	542		33	82	150	330	542
mean 1 (Å)[a]	4.4080	4.4195	4.4128	4.4151	4.4191	mean 3 (Å)	3.6491	3.6516	3.6578	3.6561	3.6490
std dev (Å)	0.1066	0.1046	0.1800	0.2289	0.2086	std dev (Å)	0.0433	0.0620	0.0931	0.0792	0.1631
mean 2 (Å)	5.1161	5.1138	5.1129	5.1175	5.1242						
std dev (Å)	0.2053	0.2989	0.2998	0.3536	0.3368						

(b) RHO Framework: An 8-Ring System

	temp (K)						temp (K)			
	80	134	331	552		80	134	331	552
mean 1 (Å)[b]	6.6721	6.6718	6.6676	6.6712	mean 3 (Å)	6.6576	6.6569	6.6520	6.6553
std dev (Å)	0.0815	0.1019	0.1487	0.2095	std dev (Å)	0.0839	0.0919	0.1318	0.1769
mean 2 (Å)	7.0521	7.0450	7.0572	7.0517	mean 4 (Å)	6.6397	6.6372	6.6300	6.6309
std dev (Å)	0.2780	0.2717	0.3616	0.2764	std dev (Å)	0.0622	0.0880	0.1284	0.1788

(c) TON Framework: A 10-Ring System

	temp (K)						temp (K)			
	30	60	300	560		30	60	300	560
mean 1 (Å)[c]	8.5432	8.5403	8.4861	8.4988	mean 4 (Å)	6.3338	6.3370	6.3609	6.3247
std dev (Å)	0.0681	0.0909	0.1788	0.1939	std dev (Å)	0.0276	0.0443	0.0971	0.3629
mean 2 (Å)	8.5445	8.5413	8.5855	8.5696	mean 5 (Å)	8.0133	8.0156	7.9991	8.0387
std dev (Å)	0.0636	0.1011	0.1642	0.2064	std dev (Å)	0.0652	0.0991	0.1944	0.2100
mean 3 (Å)	6.3339	6.3367	6.3727	6.3854					
std dev (Å)	0.0286	0.0447	0.0986	0.1371					

(d) MFI Framework: A 10-Ring System

	temp (K)						temp (K)			
	30	80	300	550		30	80	300	550
mean 1 (Å)[d]	8.0730	8.0758	8.0853	8.1011	mean 4 (Å)	8.4382	8.4266	8.3841	8.3507
std dev (Å)	0.0451	0.0724	0.1271	0.1691	std dev (Å)	0.0535	0.0841	0.1432	0.1901
mean 2 (Å)	8.1513	8.1449	8.1293	8.1227	mean 5 (Å)	7.9947	8.0095	8.0628	8.1104
std dev (Å)	0.0495	0.0769	0.1263	0.1780	std dev (Å)	0.0455	0.0748	0.1254	0.1707
mean 3 (Å)	8.0715	8.0767	8.0873	8.1076	mean 6 (Å)	8.1822	8.1820	8.1901	8.1893
std dev (Å)	0.0429	0.0679	0.1227	0.1596	std dev (Å)	0.0570	0.0922	0.1619	0.1892

(e) LTL Framework: A 12-Ring System

	temp (K)						temp (K)			
	30	80	300	550		30	80	300	550
mean 1 (Å)[e]	10.1038	10.1123	10.1364	10.1607	mean 2 (Å)	10.5742	10.5795	10.5982	10.6053
std dev (Å)	0.0434	0.0537	0.0990	0.1191	std dev (Å)	0.0642	0.0487	0.1081	0.1507

(f) LTL Framework (Silica Composition Structure): A 12-Ring System

	temp (K)						temp (K)			
	30	80	300	550		30	80	300	550
mean 1 (Å)[f]	10.3036	10.3120	10.3364	10.3489	mean 2 (Å)	10.3912	10.3967	10.4189	10.4270
std dev (Å)	0.0441	0.0666	0.0959	0.1237	std dev (Å)	0.0614	0.0749	0.1083	0.1305

(g) *BEA Framework: A 12-Ring System

	temp (K)						temp (K)			
	30	60	300	560		30	60	300	560
mean 1 (Å)[g]	10.8350	10.8318	10.8111	10.7950	mean 4 (Å)	8.7408	8.7423	8.7445	8.7387
std dev (Å)	0.0777	0.1058	0.1645	0.2001	std dev (Å)	0.0462	0.0653	0.1096	0.1815
mean 2 (Å)	8.7412	8.7426	8.7445	8.7433	mean 7 (Å)	8.2983	8.3047	8.3287	8.3450
std dev (Å)	0.0470	0.0666	0.1148	0.1607	std dev (Å)	0.0446	0.0721	0.1187	0.1679
mean 3 (Å)	10.8365	10.8321	10.8126	10.8030	mean 8 (Å)	8.3001	8.3045	8.3276	8.3490
std dev (Å)	0.0683	0.1005	0.1717	0.1968	std dev (Å)	0.0441	0.0685	0.1181	0.1692

[a] Distance between those oxygen atoms that in the initial, symmetric geometry of space group $Im\bar{3}m$ (No. 229) are generated from O_1 at 0.0000, 0.6475. 0.6475 by the operations $^1/_2+x,^3/_2-y,^3/_2-z$ and $^1/_2+y,^3/_2-z,^1/_2+x$ (distance 1; across the 6-ring). $y,1-z,x$ and $x,1-y,z$ (distance 2: across the 6-ring), $1-y,z,x$ and $y,1-z,x$ (distance 3: across the 4-ring). [b] Distance across the 8-ring aperture between those oxygen atoms that in the initial, symmetric geometry of space group $Im\bar{3}m$ (No. 229) are generated from O_1 at 0.2753. 0.1197, 0.5000 and O_2 at 0.1653. 0.1653, 0.3695 by the following operations—O_1: $z,1-x,1-y$ and O_1: $1-z,x,1-y$ (distance 1): O_2: $^1/_2+x,^1/_2-y,^1/_2+z$ and O_2: $^1/_2-x,^1/_2+y,^1/_2+z$ (distance 2): O_1: $x,z,1-y$ and O_1: $1-x,z,1-y$ (distance 3); O_1: $z,1-y,x$ and O_1: $1-z,1-y,1-x$ (distance 4). [c] Distance between those oxygen atoms that in the initial, symmetric geometry of space group $Cmc2_1$ (No. 36) are generated from O_2 at 0.0942. 0.2224. 0.2068 and O_3 at 0.2712, 0.3789. 0.6639 by the following operations—O_2: $^1/_2+x,^1/_2-y,^1/_2+z$ and O_2: $^1/_2-x,^1/_2+y,z$ (distance 1: across the 10-ring): O_2: $^1/_2+x,^1/_2+y,z$ and O_2: $^1/_2-x,^1/_2-y,^1/_2+z$ (distance 2: across the 10-ring); O_3: x,y,z and O_3: $1-x,y,z$ (distance 3; across the 6-ring): O_3: $x,1-y,z-^1/_2$ and O_3: $1-x,1-y,z-^1/_2$ (distance 4; across the 6-ring): O_3: $1-x,y,z$ and O_3: $x,1-y,z-^1/_2$ (distance 5: across the 10-ring). [d] Distance across the 10-ring aperture between those oxygen atoms that in the initial, symmetric geometry of space group $Pnma$ (No. 62) are generated from O_1 at 0.3726, 0.0534, −0.2442. O_2 at 0.3084. 0.0587. −0.0789. O_7 at 0.3742, −0.1561, −0.2372. O_8 at 0.3085. −0.1552. −0.0728. O_{18} at 0.1886. 0.1298. −0.3836. O_{20} at 0.1951. −0.1291. −0.4190. O_{21} at −0.0037, 0.0502. −0.2080. O_{22} at −0.0040. −0.1528. −0.2078. O_{24} at 0.1884. −0.2500. −0.3538. and O_{26} at 0.1085, −0.2500. 0.0611 by the following operations—O_{21}: $^1/_2+x,y,^1/_2-z$ and O_{22}: $^1/_2-x,-y,^3/_2+z$ (distance 1); O_2: $x,y,1+z$ and O_8: $1-x,-y,1-z$ (distance 2): O_{21}: $1+x,y,1+z$ and O_{22}:

Footnotes for Table II (*continued*)

1-x,-y,-z (distance 3); O_1: $^1/_2+x$,y.$^1/_2-z$ and O_7: $^3/_2-x$.-y,$z+^1/_2$ (distance 4): O_{24}: x.1+y,1+z and O_{26}: x,1+y,z (distance 5); O_{20}: x,1+y,1+z and O_{18}: $^1/_2-x$,$^1/_2+y$,$^1/_2+z$ (distance 6). [e] Distance across the 12-ring aperture between those oxygen atoms that in the initial, symmetric geometry of space group $P6/mmm$ (No. 191) are generated from O_1 at 0.0000, 0.2754, 0.5000 and O_2 at 0.1659, 0.3318, 0.5000 by the following operations—O_1: x-y,-y.z and O_1: y.$y-x$,z (distance 1); O_2: x.y,z and O_2: $x-y$,-y,z (distance 2). [f] Distance across the 12-ring aperture between those oxygen atoms that in the initial, symmetric geometry of space group $P6/mmm$ (No. 191) are generated from O_1 at 0.0000, 0.2815, 0.5000 and O_2 at 0.1639, 0.3278, 0.5000 by the following operations—O_1: x,y,z and O_1: y,$y-x$.z (distance 1): O_2: x.y.z and O_2: $x-y$,-y,z (distance 2). [g] Distance across the 12-ring aperture between those oxygen atoms that in the initial, symmetric geometry of space group $P4_122$ (No. 91) are generated from O_{31} at 0.8354, 0.8390, 0.0607 and O_{40} at 0.8356, 0.4949, 0.0608, O_{50} at 1.000, 0.8215, 0.000 and O_{60} at 1.000, 0.5126, 0.0000 by the following operations—O_{31}: x,1-y.$^1/_2-z$ and O_{40}: x,y,z (distance 1): O_{60}: 1-y,x.$^1/_4+z$ and O_{50}: 2-y.x.$^1/_4+z$ (distance 2); O_{40}: 2-x,y,1-z and O_{31}: 2-x.1-y,$^1/_2+z$ (distance 3): O_{50}: y,x.$^3/_4-z$ and O_{60}: 1+y,x,$^3/_4+z$ (distance 4); O_{31}: 2-y.x.$^1/_4+z$ and O_{40}: 1-y,x.$^1/_4+z$ (distance 7); O_{31}: x,2-y.$^1/_2-z$ and O_{40}: x.1-y.$^1/_2-z$ (distance 8).

with substantially increased density at the $x = \pm a$ turning points. As an example of the significance of the classical–quantum distinction we examine the Debye–Waller factor in each case. In X-ray scattering the Debye–Waller factor accounts for the effect on the scattered intensity of the density distribution of the scattering centers in direct space which is equivalent to a set of delta functions convolved with individual density functions. The scattered wave function is the Fourier transform of the scattering density, with the Debye–Waller factor arising from the convolution theorem. For a quantum harmonic oscillator, the Fourier transform of the real space Gaussian is a Gaussian in reciprocal space, as actually implemented in quantitative diffraction calculations. The Fourier transform of the classical result, eq 7, however, is a zeroeth-order Bessel function of the first kind.[53] In the present case, the atom position densities are found not to be endpoint-heavy. Apparently the multibody, statistical effects that come into play between atoms separated across the zeolite pores (5–12 Å) render classical mechanics an acceptable approximation in the present case.

(53) Weast, R. C. *CRC Handbook of Chemistry and Physics*. 68th ed.: CRC Press: Boca Raton, FL, 1987; p A-83.

Conclusion

Constant volume crystal dynamics simulations of the six representative zeolite structure types SOD (sodalite; 6-ring), RHO (rho; 8-ring), TON (theta-1; 10-ring), MFI (silicalite; 10-ring), LTL (Linde type L; 12-ring), and *BEA (beta; 12-ring) reveal substantial motion of the framework atoms about their equilibrium positions. The framework flexibilities are explicitly modeled by a crystal mechanics force field with parameters taken from quantitative interpretations of Raman and infrared spectroscopic data. The mean squared atomic displacements are, as expected, substantially smaller than the upper limit afforded by diffraction results. The increased fluctuations in the effective aperture sizes with temperature depend on the framework connectivity, also consistent with experimental observation. The frequency spectra of the O–O distances across the apertures reveal that motions of the corresponding tetrahedra are coupled. The definition, extent, and period of the fluctuations depend on the framework connectivity. It is most pronounced in the SOD and RHO frameworks, previously known from experiment to be the most susceptible to static framework distortion. The change with time in cross-sectional area of the 12-ring window in the LTL framework is cyclical, at a frequency of $\sim$200 cm^{-1}, a clear and direct demonstration of breathing motion of the zeolite pores.

Electronic Structure and Reactivity of Dioxirane and Carbonyl Oxide

Robert D. Bach,*[†] José L. Andrés,[†] Amy L. Owensby,[†] H. Bernhard Schlegel,[†] and Joseph J. W. McDouall[‡]

Contribution from the Departments of Chemistry, Wayne State University, Detroit, Michigan 48202, and University of Manchester, Manchester M13 9PL, United Kingdom.
Received October 28, 1991

Abstract: Dioxirane, the diradical dioxymethane, and carbonyl oxide have been studied at a variety of levels including MP2, MP4, CASSCF, QCISD, and QCISD(T). MP2 optimization is sufficient for dioxirane, the various dioxymethane biradicals, and substituted carbonyl oxide, but optimization at the QCISD or QCISD(T) level is needed to obtain the correct structure for carbonyl oxide. Significantly, both levels of theory give essentially the same C–O/O–O bond length ratio for this controversial molecule (1.281/1.369 Å and 1.287/1.356 Å for QCISD/6-31G* and QCISD(T)/6-31G**, respectively). The unsubstituted carbonyl oxide is probably anomalously sensitive to the level of calculation, since MP2/6-31G* calculations on dimethylcarbonyl oxide afford a C–O/O–O bond ratio of 1.283/1.345 Å, consistent with the higher level calculations on the parent carbonyl oxide. Transition structures have been obtained at the MP2/6-31G* level for the isomerization of carbonyl oxide to dioxirane and for the donation of oxygen from carbonyl oxide and dioxirane to ethylene. A scan of the potential energy curves for O–O bond dissociation in hydrogen peroxide and water oxide shows that the MP4SDTQ and QCISD(T) curves are nearly superimposable for bond elongation up to 2.5 Å. At the QCISD(T)/6-31G*//MP2/6-31G* level, carbonyl oxide is 28.6 kcal/mol higher than dioxirane and separated from it by a barrier of 19.1 kcal/mol; the barriers for donation of an oxygen atom from dioxirane and carbonyl oxide to ethylene are 16.7 and 11.9 kcal/mol, respectively. The MP4SDTQ level is adequate for determining the barriers for the first two reactions, but QCISD(T) is required for a proper treatment of the barrier for dioxirane plus ethylene (MP4 overestimates the triples contribution). Theoretical evidence is presented that suggests that both the reactants and the transition structures involved in these epoxidation reactions are principally closed shell in nature.

Introduction

Although a dioxirane has only recently been isolated and characterized by Murray,[1a] earlier experimental work by Edwards and Curci[1b] stimulated the theoretical community[2] to calculate the chemical and physical properties of the parent dioxirane (**1**)

[†] Wayne State University.
[‡] University of Manchester.

(1) (a) Murray, R. W.; Jeyaraman, R. *J. Org. Chem.* **1985**, *50*, 2847. (b) Curci, R.; Fiorentino, M.; Troisi, L.; Edwards, J. O.; Pater, R. H. *J. Org. Chem.* **1980**, *45*, 4758. (c) Bunnelle, W. H. *Chem. Rev.* **1991**, *91*, 335.

0002-7863/92/1514-7207$03.00/0 © 1992 American Chemical Society